Solid Earth Discuss., doi:10.5194/se-2016-16, 2016
Manuscript under review for journal Solid Earth
Published: 5 February 2016

Solid Earth Discussions

X-ray CT analysis of pore structure in sand

Toshifumi Mukunoki[1], Yoshihisa Miyata[2], Kazuaki Mikam[3] and Erika Shiota[1]

[1] X-Earth Center, Graduate School of Science and Technology, Kumamoto University, 1-39-2 Kurokami Kumamoto-city, Kumamoto, JAPAN

[2] Department of Civil and Environmental Engineering National Defense Academy, 1-10-20 Hashirimizu, Yokosuka, JAPAN

[3] Japan Oil, Gas and Metals National Corporation, Toranomon Twin Building 2-10-1 Toranomon, Minato-ku, Tokyo, JAPAN

Corresponding author to: Toshifumi Mukunoki (mukunoki@kumamoto-u.ac.jp)

ABSTRACT

The development of a micro-focused X-ray CT device enables digital imaging analysis at the pore-scale. The applications have been diverse, for instance, in soil mechanics, geotechnical and geoenvironmental engineering, petroleum engineering, and agricultural engineering. In particular, imaging of the pore space of porous media has contributed to numerical simulations for single and multi-phase flow, or contaminant transport, through the pore structure as three-dimensional image data. These obtained results are affected by the pore diameter so it is necessary to verify the image pre-processing for image analysis, and validate the pore diameters obtained from the CT image data. Besides, it is meaningful to produce the parameters in a representative element volume (REV) and significant to define the dimension of REV. This paper describes the underlying method of image processing and analysis and discusses the physical properties of Toyoura sand for the verification of image analysis based on the definition of REV. Based on the obtained verification results, pore diameter analysis can be conducted and validated by the comparison of the experimental work and image analysis. The pore diameter was deduced by Laplace's law and the water retentively test for the drainage process. The referenced results and perforated-pore diameter proposed originally in this study, called the voxel-percolation method (VPM), are compared in this paper. The paper describes the limitation of REV, the definition of pore diameter, and the effectiveness of VPM for the assessment of pore diameter.

Key words: Pore diameter, Image analysis, REV, percolation, X-ray CT

Solid Earth Discuss., doi:10.5194/se-2016-16, 2016
Manuscript under review for journal Solid Earth
Published: 5 February 2016

1. INTRODUCTION

The estimation of pore dimensions and pore networks in soil is one of the most important studies to evaluate the mechanical and hydrodynamic properties for soil science, soil mechanics, geotechnical and geoenvironmental engineering, and petroleum engineering [Carman (1939), Brooks and Corey (1964), Topp and Miller (1966), Bear (1972), Mualem (1976), Chatzis et al. (1983), Dullien (1992), Helming (1997), Chanpus (2004), Culligan et al. (2006), Riyadh (2007), Gharbi and Nlunt (2012)]. In fact, it is difficult to define pore dimensions in grains because the pores are surrounded by grains and are thus not isolated. Figure 1 illustrates a pore in spheres. As shown in Figure 1(a), five spheres surround one pore such that the pore should be defined by nine contacting points. However, the pore space is not closed by the five spheres. The shape of soil particles is not spherical, but rather a complicated shape so the pore dimension is able to be defined based on assumption only. Figure 2 shows the X-ray CT image of a grain sample in two dimensions. The X-ray CT shows the spatial distribution of density, which enables the soil particles and pores to be distinguished. Locally, the longest and shortest length of the pore, as shown in Figure 2 (a), can be measured by using software for image analysis. However, it is partial property of the pore, and the required information is at least a property in representative volume. It should be required not to measure individual pore dimensions by using software, but to estimate them by using a systematic method. Moreover, complicated pores have an aspect ratio as shown in Figure 2, so the discussion of connectivity of pores will be required for the study of the hydrodynamic issue in soils. The challenge of this paper is to propose an evaluation method for the pore dimensions.

Here shall we look back the current technique on the pore analysis. The most popular method for measuring pores in soil is the indirect methods of the mercury intrusion technique (MIT) or the air intrusion method (AIM). These methods are based on the concept that the pore structure assumes a straight tube. Thus, the three-dimensional pore network is not an issue. Through recent developments of the scanning electron microscope (SEM) and non-destructive testing methods such as computed tomography (CT) and magnetic resonance imaging (MRI) the pore structure in soil can be measured directly. In particular, CT is applicable by using rays, for example, sound, ultrasound, x-ray and gamma ray, so that the pore structure of various engineering materials [Otani and Obara (2003), Desrues et al. (2006), Alshibli and Reed (2010) and Cnudde and Bernard (2013)] can be scanned. Additionally, advanced CT has been developed to scan in the micro scale [Altman et al.(2005), Wildenschild et al. (2002), Wildenschild et al. (2005), Wildenschild et al. (2005), Mukunoki et al. 2010, Higo et al. (2011), Wildenschild and Sheppard (2013), Andrew et al (2014), Andrew et al. (2015) and Taylor et al. (2015)]. To evaluate a structure consisting of a great number of pores, a suitable image analysis method is required.

The most popular method to evaluate the porosity of porous materials from CT is based on a statistical assumption. Parameters of the distribution function based on CT data can be determined by an optimization technique [e.g. Kato et al. (2014) and Mukunoki et al. (2014)]. The accuracy of these methods depends on the selection of distribution functions based on the CT data. The required number and type of functions are still under discussion and there may be a number of solutions to these issues.

This paper discusses the evaluation method of pore structure of sand from micro focused CT scan data. In this paper, authors distinguish pore from pore structure. In the first part of the paper, the authors propose the application of the mathematical morphology method for estimating the pores of sand. By showing the analysis results of simple subjects, the usefulness of proposed method will be validated. Next, the importance of the selection of a representative element volume (REV) is discussed for estimating the grain size distribution and the averaged pore index, such as the porosity and specific surface. The authors show there is an optimum REV in this analysis. Based on the above fundamental examination to treat CT data, the authors propose a voxel-percolation method (VPM) to evaluate the pore structure of sand. The estimated results are compared with a water retention curve test, and the effectiveness of proposed method is described. It concluded that the required resolution to evaluate the pore structure is almost equivalent to that for a pore. The final objective of this research is to develop a general method for soils. As a primary research, the evaluation of sand will be treated in this paper because it is natural material and has a uniform grain shape.

2. X RAY-CT SCAN

Table 1 lists the specifications of the micro-focused X-ray CT scanner (TOSHIBA TOSCANNER 32300 FPD) installed at the X-Earth Center at Kumamoto University in 2010. In general, 360-degree radioscopic image data, for an inspection object placed on a sample table, is obtained using an X-ray image intensifier by turning the table while irradiating the object with X-rays. This radioscopic image data is then used in reconstruction calculations, which result in cross-sectional

Solid Earth Discuss., doi:10.5194/se-2016-16, 2016
Manuscript under review for journal Solid Earth
Published: 5 February 2016

images. Because the generated X-ray beam is a polychromatic beam with a wide range of frequencies, corrections are made for the beam-hardening effect. Radioscopic images alone are not sufficient to accurately represent internal components that have a complex structure. Tomographic reconstruction allows the detection of fine flaws, foreign matter, separation, and other phenomena. State-of-the-art technology allows for high-precision and high-speed inspection, permitting new applications in various fields. Figure 3 shows an illustration of the internal view of the micro-focused X-ray CT scanner. The detector is a flat panel detector (FPD), which enables three-dimensional scanning with a cone-shaped X-ray beam. The scan speed depends on the scanning conditions. The sample was placed on the scan table and scanned with the cone-shaped X-ray beam. During scanning, the scan table was rotated to obtain a 360° scan. A back projection of the X-ray attenuation was detected on the FPD. The X-ray CT images obtained were free from the ring artifact normally seen in CT images because the scanner applied a filter function to reduce this during the image reconstruction process.

Table 2 lists the scan condition selected for this study. An of x-ray tube voltage of 60 kV and a current of 200 μA were chosen, and the focus-to-center distance (FCD) was defined as 24.7 mm; hence the dimension of one voxel is 5×5×5 μm in this study. In general, the scan condition depends on the target of study and the voltage, current and FCD should be variable. The scan conditions selected in this study are not absolute conditions, and each user has to find the best condition to observe the target in each study. Figure 4 shows the photograph of the scan setup in the micro-focused X-ray CT room. To obtain high-resolution images, the specimen must be in close proximity to the X-ray tube, as shown in Figure 4. The soil tested was Toyoura sand with a dry density of 1.57 t/m^3 (i.e., the porosity was 0.41). The sample was well packed into an acrylic mold with a diameter of 10 mm and a thickness of 1 mm. If the diameter of the specimen is greater than 10 mm, for example 20 - 30 mm, the center of the specimen is too far from the X-ray tube and high-resolution CT images cannot be obtained because of the loss of focus distance between the X-ray tube and the center of the specimen.

3. IMAGE PROCESSING OF A PORE IN SAND BASED ON X-RAY CT DATA

3.1 Outline of image processing of a pore in sand

There may be some methods of treating image processing of a pore in sand from X-ray CT data. In this paper, the applicability of mathematical-morphology is discussed. The

Solid Earth Discuss., doi:10.5194/se-2016-16, 2016
Manuscript under review for journal Solid Earth
Published: 5 February 2016

Solid Earth
Discussions
Open Access

mathematical-morphology shows the complicated form by using element whose dimension is known [Soille (2003)]. The basic operations are available in many image analysis software packages [Luis et al. (2005)]. The pore has a complicated form so this concept may be useful for evaluation.

The basic process for image analysis in this study is as follows:

1) Image segmentation to create a binary image from an original image (3.1.1);
2) Determination of pore diameter using a granulometric method based on mathematical morphology (3.1.2);

3.1.1 Image segmentation

As the first step of image analysis, the pore and grain are identified from CT-data. For the operation, the image segmentation method developed by [Otsu (1979)] was used because the Toyoura sand tested showed two distinct peaks in this study. Two peaks of CT values indicate the two phases of particles and pore space, respectively. During this process, the binary data is set such that the grain is black and the pore is white. By determining the voxel number for each region, the averaged index showing the pore, such as the void ratio, can be evaluated. However, by this process, the distribution of the pores according to size cannot be evaluated.

3.1.2 Granulometric method

In the second step of image analysis, for each pore which is identified by binary data, the shape is evaluated by using mathematical morphology. Based on this concept, unit element B belongs to a pore X. Then the unit element in X, B_x, can be written by following equation.

$$B_X = B \cup X \qquad (1)$$

It is likely that the shape of unit element is a square or a circle with a symmetric shape. In this study, the target subject is a pore and the interest is its size. Obtaining the image of a pore from the X-ray CT scanner, the dimensions of the pore can be shown by using the unit element, because dimension of the unit element can be regulated. In this study, the unit element of a sphere is used, thus the element is called the sphere element in this paper.

Figure 5 illustrates the sphere element. In this study, thirteen sizes of sphere element are used. In

Solid Earth Discuss., doi:10.5194/se-2016-16, 2016
Manuscript under review for journal Solid Earth
Published: 5 February 2016

this figure, the first three elements are shown. The number of the maximum sphere element used as a radius is r=13 in this study. The smallest element is one voxel (Figure. 5(a)). Elements with a lower sphere number do not appear exactly spherical in shape. However, the greater the number of voxel for diameter of structural element, the more it spherical it becomes, as shown in Figure 5. The voxel number as a diameter of a sphere element, D can be defined as per following equation:

$$D=2r+1 \quad r \geq 0 \qquad (2)$$

where r is a voxel number from the center of the sphere element. As shown in Figure 5, when r is 1, which is the minimum number, d is 3; therefore, the diameter of sphere element is 3. The diameter increased based on the center inclusion concept, so the diameter of the sphere element should be always an odd number. The more r increases, the more the shape of the sphere structure l becomes spherical. For the generation of a sphere element with different dimension, Image Tool Kit called ITK [Luis et al. (2005)] was used.

The granulometric method can recreate the complicated pore space by overlapping sphere elements with several different diameters. Initially, the smallest sphere element, i.e., one voxel, should be applied to the analysis area, which is a pore space, and it should occupy the entire pore space. Then, the next sphere element with a diameter of 3 voxels, as shown in Figure 5, is applied same area of pore space, but the next sphere element cannot occupy the entire pore space. Likewise, the entire pore space is scanned by each sphere element and the more complicated the pore shape, the more sphere elements with different diameter will be required. In the granulometric method, the sphere element is overlapped partially; hence, the distribution of pore diameter indicates that the non-overlapped part of sphere element is evaluated by the voxel number. In addition, the summation of the overlap ratio of the sphere element at each step can be used to evaluate the pore volume and saturation degree by the voxel percolation method, explained in the following section.

3.2 Verification of image processing for simple objects

Figure 6(a)-(e) explains the features of the granulometric method. Figure 6(a) and (b) illustrate a circle and a square rotated 45° in the dimension of 200 x 200 (i.e. the total voxel number is 40000), and Figure 6(c) prepares the circle and square in the dimension of 400 x 200 (i.e. the total voxel number is 80000). Let us define the space other than the circle and square as pore space. It is noted that authors refer to a sphere element as a circle element in this section because the target subject is

Solid Earth Discuss., doi:10.5194/se-2016-16, 2016
Manuscript under review for journal Solid Earth
Published: 5 February 2016

drawn in two dimensions. At the end of the image analysis using the granulometric method, herein referred as granulometric image analysis (GIA), authors can count the number of voxel involved in each sphere element. All images classified by each sphere element, as shown in Figure 6, were overlapped in the order of the diameter of the circle element. The number of voxel for a minimum circle element is equal to the number of pore structure in total. Hence, the number of voxel for circle element greater than the minimum circle element should be less than the number of pore spaces. Finally, all circle elements are overlapped due to the radius of the circle element and the total number of voxel is same as that of the pore space, as shown in Table 3; and then, it can be expressed by the following set equation;

$$S = \sum_i^n B(r_i) - \sum_i^n \{B(r_i) \cap B\,(r_{i+1})\} \quad i=0,\ 1,\ 2 \ldots . n \quad (3)$$

where S is the number of voxel as area/volume counted by GIA, $B(r_i)$ is area/volume of the circle/sphere element with a radius from i to n. When i is n, S is equal to the target area/volume. Even if the shape of the pore space is complicated, as in Figure 6(c), GIA can estimate the voxel number in total. Note that each circle element labeled and its location were also recoded; hence, the spatial distribution of the overlapped circle element can be visualized as shown in Figures 6. Here, it should be recognized that the diameter of the circle element cannot become a pore diameter directly. Hereby, a definition of pore diameter is required.

If the diameter of sphere element is equivalent to the pore diameter, its pore geometry must be a set of parallel lines or a rectangular shape. The area in dotted lines, as shown in Figures 6 (d) and (e), was analyzed by GIA and both areas were found to be 19801. For latter case, the two artificial images in Figures 6(d) and (e) can provide an interesting discussion. Certainly, GMI estimates the width in the area of the diamond; despite the fact that the definition of width is vague, GMA produced Figure 6(d). Even if the target image is rotated by 45° , the same results should be obtained. GMA searches the minimum pore space first and then, the sphere element with the diameter due to order of odd number becomes larger. The point is the sphere element evaluates the space at four corners, as shown in Figure 6(e). This result indicates the important feature of this image analysis; in short, the sphere element finds small pore spaces and evaluates the diameter by the part remaining after the overlapping process. This behavior, whereby the sphere element finds the small space, is similar to capillary behavior in porous materials such as sand.

3.3 Selection of appropriate Representative Element Volume (REV) for analysis of sand

Solid Earth Discuss., doi:10.5194/se-2016-16, 2016
Manuscript under review for journal Solid Earth
Published: 5 February 2016

The representative element volume (REV) of the subject should be discussed to estimate the geometrical properties of sand by image analysis. In this study, the porosity and specific surface of Toyoura sand were evaluated, and their REV was assessed. Detailed steps can be referred from [Fujiki et al. (2014)]; hence, the concept is only introduced in this paper as follows:

1) Sub-sampling region is defined by the authors;
2) The porosity and specific surface are calculated from the CT-image;
3) Their mean-value and standard deviation of the porosity (n) and specific surface (S_{sp}) defined by the following equations are calculated; and then,

$$n = \frac{V_{pore}}{V_t} \qquad (4)$$

$$S_{sp} = \frac{S_{ps}}{V_t} \qquad (5)$$

where V_{pore} is a volume of pore, V_t is the total volume of specimen and S_{ps} is mean-surface of grains obtained from CT image.
4) The process from the above items 1 to 3 is continuously repeated due to the enlargement of the calculation region until reaching the relative standard deviation (RSD) which is defined by the equation expressed as the standard deviation divided by mean-value, isless than 1%.

Figures 7(a) and (b) show the two-dimensional images of particles of Toyoura sand in each square dimension. The dimension of the CT image of Figure 7(a) is 1024 x 1024; however, if the extraction of the cubic area from this CT image is required, the maximum voxel number to be used is 700, as shown in Figure 7 (a). These images can be obtained from binary images following the image segmentation process. In this study, the Ohtsu method was applied to create binary images. For each three-dimensional image, the porosity and specific surface were evaluated to validate the representative volume. The measured porosity of the specimen was 0.44, and the analyzed porosity was 0.431, so both values were a good fit. Figure 8 presents the evolution of the relative standard deviation (RSD) for the porosity and specific surface with a sub-sample size. A theoretical decreasing behavior is observed for both cases. The behavior observed for the two cases generally results in close values. The difference between the porosity and the specific surface is not significant for the tested materials but, generally, the REV should depend on the medium property.

Figure 9 shows the distribution curves of the grain size obtained from the sieving test and image analysis. The grain size distribution curve by image analysis can be obtained from Image J, which is provided using the function of object counter. With the exception that the image analysis area is cubic of 100 voxels, the grain size distribution obtained from the CT image has a good fit to the results of the sieving test. Figure 10 shows the relationship between the image analysis area and the particle diameters analyzed. The subscript number D means the percentage value finer, by weight, obtained from Figure 9. The Figure 10 results show that a cubic area of more than 300 voxels can provide a constant grain size for each percentage finer by weight. Defining a limit for the RSD in order to choose the size L of the REV remains an open question. The orders of magnitude are summarized in Table 4. The effect of the size of the reference sample is not significant. This observation supports the fact that the 300 voxel size (or 1.5 mm size) sample is larger than the REV when one voxel size is 5 μm.

4. ANALYSIS METHOD OF PORE-STRUCTURE

4.1 Pore structure analysis

In the process of section 3.2, GIA produces pore by the overlapping of many sphere elements. In this chapter, pore structure analysis based on GIA is described. It is important to consider three-dimensional continuity of the pore in analyzing the pore structure. In this paper, the pore structure analysis method to perform vertical air-entry simulation with the imaged pore from X-ray CT data is proposed. This method is called the voxel-percolation method (VPM) in this paper. For instance, the number of the kind of sphere element is 13, as shown in Figure 11. For convenience, the images in Figure 11 are drawn in two dimensions; therefore, sphere elements should be called circle elements in the explanation of Figure 11. In order to start the percolation flow simulation, in this study, the rule for water-drainage process should be as follows:

Step 1: The original image is binarized to pore space (white) and soil particles (black) (see Figure 11(a));

Step 2: The pore space is analyzed by GIA, and thus the distribution of the labeled sphere element can be known (Figure 11(b));

Step 3: VPM starts to find the labeled voxel (herein as 13) of the circle element with the largest radius from the corner of the defined side. As in Figure 11(c), only the area of the sphere element with a radius of 13 is shown as white.

Step 4: Once VPM finds the labeled voxel of 13, it will keep painting those voxels until it recognizes no continuous circle element (Figure 11(c)-(o)). Likewise, the labeled number

Solid Earth Discuss., doi:10.5194/se-2016-16, 2016
Manuscript under review for journal Solid Earth
Published: 5 February 2016

of the largest sphere element is scanned to the image treated in Step 2, and so only the voxel corresponding to the largest sphere element is counted. Step 3 should be repeated until the smallest sphere element is used;

Step 5: The results in Step 4 produce the saturation degree by the summation of the counted voxel divided by the number of voxels of the entire pore; and

Step 6: The capillary pressure can be evaluated by using Young-Laplace's equation with the diameter of the sphere element.

4.2 Analyzed water retention curve

The water retention property of a soil is a typical parameter influenced by pore structure. In this section, the water retention curve can be reproduced by combining GIA and VPM. Based on section 4.1, the water retention curve (WRC): h_p-S_r for the drainage process can be drawn. Figure 12 shows the 3D image of the percolation flow. As a first step, VPM gave the distribution of the connecting sphere elements with different size, and then, all voxels with sphere elements share the same label. By sharing same label, the behavior of voxel seems to flow, as shown in Figure 12(a) – (f), and this is percolation flow. Figure 13 shows the occupation ratio of the cumulative volume of the sphere element. In fact, the occupation ratio of the cumulative volume of the sphere element countervails the volume ratio of air in the pore structure, and so the saturation degree can be evaluated by subtracting the cumulative volume of the sphere elements from the entire pore volume. This can be expressed by:

$$S_r = 1 - \frac{\sum_i^n B_i - \sum_i^n B_i \cap B_{i-1}}{V_T} \qquad (6)$$

where V_T is a volume of entire pore structure. The diameter of sphere element at each step contributes to the calculation of capillary pressure head (h_p) by the Young-Laplace equation as shown in eq. (7):

$$h_p = \frac{4T\cos\theta}{\gamma_w d} \qquad (7)$$

where T is the surface tension between the water and air (72.88 mN/m at 20^{o}C), θ is the contact angle (49^{o}) , γ_w is the density of water, and d is the diameter of the tube.

In this study, the WRC test for the drainage process could be performed so it was simulated by the

Solid Earth Discuss., doi:10.5194/se-2016-16, 2016
Manuscript under review for journal Solid Earth
Published: 5 February 2016

following treatments.

1) To label each sphere element categorized and to recognize the label number of the sphere element with the maximum diameter;
2) To count the number of voxel with the label number corresponding to the maximum diameter from the direction of air entry side, and it should be continued until the discontinuous condition, as shown in Figure 12(a) – (f);
3) The first item yields the capillary pressure head using the Young-Laplace equation with the substitution of the latest perforated diameter. The second item yields the saturation degree by dividing the number of voxel not counted by the total number of pore spaces. This can be plotted on one WRC.
4) Once the counting process on the above second item is finished, the next label of sphere element should be checked based on same process as item 1), 2) and 3); and lastly, the WRC can be created. In order to verify the perforated pore diameter, WRCs were obtained from the experiment at 20 ^{o}C, and image analysis was evaluated in this study.

4.3 Water retentively test to verify pore structure analysis

In this study, a water retentively test with a reducing elevation head method (WRT-REHM) was selected to conduct water drainage tests because it was available to measure the moisture content of identical specimens at different elevations head during the water drainage process. The specimen used for WRT-REHM was identical to the scanned sample. Figures 14(a) and (b) show photographs of the set-up used for the water drainage test system with a suction method, and Figure 14(c) illustrates the cross-sectional view of a mold that was tested. The mold is made of an acrylic, through which an X-ray beam could be transmitted without strong beam-hardening. The dimensions of the mold were: height of 120 mm, inner diameter of 10 mm and a thickness of 1 mm. In order to measure the amount of drained water, a glass syringe was used with a scale of 0.01 ml. A membrane filter with a mean-pore diameter of 0.2 μm was placed on a glass filter with a pore diameter between 20 and 30 μm installed on the bottom of the mold. Table 1 summarizes the specification of the soil tested. All test procedures are listed as follows:

1) The mold was filled with de-aired water and an entire system with a syringe, tube connected between the mold and syringe, glass filter, and membrane sheet was fully saturated in the storage mold under vacuum condition.

Solid Earth Discuss., doi:10.5194/se-2016-16, 2016
Manuscript under review for journal Solid Earth
Published: 5 February 2016

2） Toyoura sand was carefully installed in the mold filled with de-aired water.

3） The sand specimen was left for 24 hours after the regulation of the elevation head of the syringe to lead water drainage at each saturation degree, and then the volume of the syringe was recorded.

4） Items 3) and 4) were repeated until no water drainage was observed.

The entire test system was set up in the room with the installed micro-focused X-ray CT scanner, and the temperature was controlled at 20∓2^{o}C. Due to a change of temperature within the range of 20∓2^{o}C, the authors were concerned about the generation of condensation in the mold and extra evaporation from the specimen surface, so the humidity in the room was regulated. In the trial test, the authors monitored the time to reach a steady condition of the specimen through the checking of the fluid volume in the syringe, and it was concluded that this time should be 24 hours in this test.

4.4 Verification of pore structure analysis

Figure 15 shows the binary 3-D image of the pore space of Toyoura sand based on the method explained in section 3.1. In this figure, soil particles are invisible. Figure 16(a) to (e) show binarized X-ray CT images obtained from Figure 16 in two dimensions after GIA using 13 different sphere elements; and Figure 16 (f) is the final analysis results by overlapping each result. White represents pore space and black represents the soil particles. Eventually, this image processing was conducted in three dimensions so a 3D map can be obtained, as shown in Figure 17. Visually, each color element is distributed uniquely, as shown in Figure 17. Two neighboring elements from the 3D map are found to have neighboring colors in the color bar. That is pore size distribute continuously. From the view point of hydraulic behavior, local velocities of pore water are always different at each pore.

Figure 18 shows X-ray CT images with respect to air intrusion, obtained from the VPM analysis in 300 voxel dimensions at each capillary pressure analyzed by equation (5) with a diameter of a sphere element. The number of voxel count produced the saturation degree (Sr); hence, the water retention curve (WRC) for drainage can be obtained as an image-analyzed curve. Figure 19 presents the comparison of the saturation degree obtained from Figure 18 and that from the Toyoura sample, and thus the analyzed saturation degree was verified by Figure 19. Figure 20 shows the WRC analysis results for five voxel dimensions. Refer to Figure 5(b) to determine the effect of voxel number on analysis results. Authors validated the effect of the voxel dimension to

WRC. In Figure 20, the test result obtained from the laboratory test is also plotted. Focusing the effect of the voxel dimension as REV, when Sr is greater than 0.8, it is observed that the lower voxel dimensions yields a 50% underestimation of the measured data to an air entry pressure as a result of decrease in Sr, remarkably. In this case, as shown in Figure 18, the voxel dimension of 100 is not sufficient to become REV for the WRC evaluation where Sr is greater than 0.8; however, there is no difference between the voxel dimensions where Sr is less than 0.5. Providing the voxel dimension is more than 300 based on all issues discussed, VPM could provide a reasonable pore diameter and the authors concluded that the diameter of the sphere element can become the pore diameter.

Despite the small change in capillary pressure between 30 and 40 cm, S_r decreased from 0.9 to 0.3. This behavior indicates that mean pose size caused a capillary pressure head of 30-40 cm is mainly distributed. This behavior should be caused by sands with a value less than the uniform coefficient.

4.5 Discussion

The studies which require pore structure, are fluid mechanics, geoenvironmental engineering and petroleum engineering [Blunt (2001), Blunt et al. (2002), Blunt et al. (2013), Mostaghimi et al. (2013) Iglauer et al. (2013) and Muljadi et al. (2015)]. The issues of how to model migration of oil in porous media such as rocks/soils, and how to inject air for remediating contaminated soil by fuels, require that the water/oil flow in the soil quantitatively understands the pore structure [Morrow and Songkran (1981), Parker et al. (1987), Pantazidpou and Sitar (1993), Mayer and Miller (1993) and Soga et al. (2003)]. Normally, the distribution of pore diameters should be required to evaluate the water retention curve (WRC) as a hydraulic property of soils. The mercury intrusion technique (MIT), scanning electron microscope (SEM), and the air intrusion method (AIM) [Sato et al. (1992), Kamiya et al. (1996) and Uno et al. (1998)] have been used to measure the pore diameter. In general, MIT is used for the evaluation of pore size in clay, so Sato et al. (1992), and Kamiya et al. (1996) attempted to develop the method to evaluate pore size in sandy soil. Uno et al. (1998) included the moisture characteristic property in the results obtained from AIT [Kamiya et al. (1996)], and proposed the moisture characteristic curve method (MCCM). The measurement principle of AIM is similar to that of MIT and the obtained pore size is evaluated as the diameter of a pipe; however, the water contents were not measured. Uno et al. (1998) deduced the capillary pressure head using the Darcy's equation for air permeation, and then they evaluated the pore size based on a pipe model [Kamiya et al. (1996)]. WRC is composed of a saturation

Solid Earth Discuss., doi:10.5194/se-2016-16, 2016
Manuscript under review for journal Solid Earth
Published: 5 February 2016

degree and capillary pressure head measured by the head method with suction, or given by Young-Laplace's law with a diameter of a pipe as the representative pore diameter. AIM gives the statistic distribution of a pore diameter model of sandy soil as a glass tube. In short, the pore diameter is defined as the diameter of the tube as per implicit agreement in a number of papers.

Figure 21 is a distribution curve of a perforated pore diameter for Toyoura sand and the pore diameter deduced by the air intrusion method (AIM) proposed by Uno et al. (1998). Figure 22 presents the relationship between the image analysis area and the perforated pore diameter in this study. Figure 22 verifies that the cubic area of more than 300 voxels can provide the constant perforated pore diameter for each percent finer by volume. Hence, the results analyzed in a cubic of 300 voxels is compared with Uno et al. (1998). Figure 23 presents the comparison between the pore diameters deduced by Uno et al. (1998) and those of the authors. For interest, the measured results between 0.065 mm and 0.85 mm have a better fit than those between 0.03 and 0.055 mm. This indicates that the AIM had an overestimation of between 0.03 and 0.055 mm, and these results raise a question that the pore diameter obtained from AIM is not a Poiseuille distribution.

VPM also evaluates the connectivity of the pore space. GIA provides not only the voxel number of the sphere element, but also the spatial distribution with VPM. AIM can also provide the pore diameter as an inner diameter of the pipe, but not the spatial distribution of the pore diameter. This issue indicates that VPM has the great advantage of being able to estimate WRC. In fact, the distribution curve in Figure 21 can provide a pore size distribution function (PDF) with respect to the perforated pore diameter. PDF can also provide the saturation degree by summation of the voxel and diameter of the sphere element. Figure 24 presents the WRC analyzed by VPM and PDF in this study The WRC obtained from PDF was far from the results of VPM in terms of measured plots. This issue poses the definition of pore diameter. As described in section 4.1, VPM considers percolation using cluster labeling based on the connectivity of pore spaces. On the other hand, PDF cannot provide the percolation property. Figure 24 concluded that a reasonable WRC can be obtained from saturation degree and distribution of pore diameter concerned the percolation property. Therefore, it is significantly useful that GIA and VPM can estimate the water retention property based on the geometry of the pore structure without performing a WRC test.

5. CONCLUSIONS

In this study, a specimen of Toyoura sand was scanned using a micro-focused X-ray CT scanner,

Solid Earth Discuss., doi:10.5194/se-2016-16, 2016
Manuscript under review for journal Solid Earth
Published: 5 February 2016

and the 3D spatial distribution of a sphere element as the pore diameter (*d*) was visualized and evaluated quantitatively by granulometric image analysis (GIA). The GIA was a useful image analysis method to evaluate pore diameter in a 3-D CT image. Moreover, the voxel percolation method (VPM) was newly developed in this study, and its validation was assessed by comparing the analyzed WRC with measured results. The key conclusions are summarized as follows:

1) The size of a voxel affected the results of image analysis. When the cubic size of one voxel was 5 x 5 x 5 μm, the representative element volume (REV) to evaluate the physical property of grain materials, which are similar to Toyoura sand, was at least 300 voxels for the evaluation of grain size, porosity, surface area and perforated pore diameter. In particular, it was possible for the porosity and surface area to evaluate the relative standard deviation less than 1 %;

2) Results of GIA show that the perforated pore diameter was less than the pore diameter from the air intrusion method (AIM), and was less than 0.068 mm, meanwhile mostly similar pore diameters were evaluated near 0.085 mm. Hence, AIM provided partially different pore diameters from the results of GIA. This issue revealed that the pore diameter obtained from AIM was not Poiseuille distribution.

3) AIT can estimate pore diameter as a diameter of a pipe and the occupation ratio; however, the spatial information was not included and therefore, it was difficult to assess the water retention curve (WRC) based on pore diameter and its occupation ratio. Meanwhile, the newly proposed “voxel percolation method (VPM)” in this study can distinguish each sphere element by labeling the number based on the diameter of the sphere element and scanning the continuous label. As a result, the connectivity with complex pore spaces can be concerned and therefore, it was available for VPM to provide the WRC close to the measured result.

4) It was concluded that the VPM was the better image analysis method, which could estimate the water retention property due to drainage by percolation using cluster labeling (i.e. pore space) and capillary pressure head based on the Young-Laplace equation, as long as image data of the pore space was obtained by micro-focused X-ray CT scanner.

The second, third and fourth conclusions are based on the first conclusion. An appropriate dimension for image analysis should be defined based on the particle diameter and voxel size. In the case using the micro-focused X-ray CT scanner, the greater resolution required, the smaller the sample that should be scanned. In future work, it will be necessary to verify the appropriate dimension (i.e. REV) for several kinds of grains.

ACKNOWLEDGEMENT

This research was supported by a Grant-in-Aid for Scientific Research (C) No. 26420483. Authors thank Prof. Laurent Oxarango, who is an associate professor of University of Joseph Fourie, for his precious comment. We also thank Ms. Hitomi Miyahara, Chiaki Nagai and Yusaku Fujiki, who were a former bachelor and graduate school students of Kumamoto University, and Mr. Toru Yoshinaga and Mr. Takahiro Yoshinaga, who are technical staffs of X-Earth Center, for their sincere contribution to this research.

REFERENCES

Alshibli, A. K. and Reed, H. A. edt.(2010), "Advances in Computed Tomography for Geomaterials", Proc. of GeoX2010, ISTE, WILEY

Altman, J. S., Peplinski, J. W. and Rivers, L. M. (2005), "Evaluation of synchrotron X-ray computerized micro tomography for the visualization of transport processes in low-porosity materials", Journal of Contaminant Hydrology, 78, pp. 167-183.

Andrew, M., Bijeljic B. and Blunt, J. M. (2014), "Pore-by-pore capillary pressure measurements using X-ray microtomography at reservoir conditions: Curvature, snap-off, and remobilization of residual CO_2", Water Resource Research, 50, pp. 8760-8774. Doi:10.1002/2014WR015970.

Andrew, M., Bijeljic B. and Blunt, J. M. (2015), "Reservoir condition pore-scale imaging of multiple fluid phase using x-ray microtomography", Journal of Visualized Experiment, 96, e52440, doi:10.3791/52440.

Bear, J. (1972), "Dynamics of fluids in porous media", Dover Publications Inc., pp. 439-573.

Blunt J.M., Jackson, D. M., Piri, M. and Valvatne, H. P. (2002), "Detailed physics, predictive capabilities and macroscopic consequences for pore-network models of multiphase flow", Advances in Water Resources, 25, pp. 1069-1089.

Blunt, J.M. (2001), "Flow in porous media – pore-network models and multiphase flow", Current Opinion in Colloid & Interface Science, 6, pp. 197-207.

Blunt, J.M., Bijeljic, B., Dong, H. Gharbi., O., Iglauer, S., Mostaghimi, P., Paluszny, A. and

Pentland, C. (2013), "Pore-scale imaging and modelling", Advances in Water Resources, 51, pp. 197-216 (http://dx.doi.org/10.1016/j.advwatres.2012.03.003).

Brooks R. H. and Corey A. T. (1964), "Hydraulic properties of porous media", Colorado State Univ., Hydrology Paper, 3, pp.27.

Carman, P. C.(1939), "Permeability of saturated sands, soils and clays", The Journal of Agricultural Science, 29(2), pp. 262-273.

Chanpuis, R. P. (2004), "Predicting the saturated hydraulic conductivity of soils: a review", Bulletin of Engineering Geology and the Environment, August 2012, 71(3), pp. 401-434.

Chatzis, I. Morrow, N., and Lim, H. (1983), "Magnitude and detailed structure of residual oil saturation", Old SPE Journal, 23(2), pp. 3311-3326.

Cnudde, V. and Bernard, D. edt. (2013), "Tomography of materials and structures", Proc. of 1st International Conference on Tomography of Materials and Structures; ICTMS 2013, July 1-5 (Ghent, Belgium).

Culligan, K, Wildenschild, D., Christensen, B., Gray and W., Rivers, M. (2006), "Pore-scale characteristics of multiphase flow in porous media: A comparison of air–water and oil–water experiments", Advances in Water Resources, 29(2), pp. 227-238

Desrues, J., Viggiani, G., and Besuelle, P. edt. (2006), "Advances in X-ray Tomography for Geomaterials", Proc. of the 2nd International Workshop on X-ray CT for Geomaterials, GeoX 2006.

Dullien F.A.L. (1992), "Porous media fluid transport and pore structure", ACADEMIC PRESS, INC., pp. 132-138.

Fujiki, Y., Nagai, C., Oxarango, L. and Mukunoki, T. (2014), "Representative elementary volume determination using x-ray computed tomography", Proc. of 13th Global Joint Seminar on Geo-Environmental Engineer,pp.64-70.

Gharbi, O. and Nlunt, J.M. (2012), "The impact of wettability and connectivity on relative permeability in carbonates: A pore network modeling analysis", Water Resource Research, 48, W12513, doi:10.1029/2012WR011877

Helming, R. (1997), "Multiphase Flow and Transport Processes in the Subsurface," Springer-Verlag, Berlin Heidelberg.

Higo, Y., Oka, F., Kimoto, S., Sanagawa, T., and Matsushima, Y. (2011), "Study of strain localization and microstructural changes in partially saturated sand during triaxial tests using micro focus X-ray CT", Soils & Foundations, 51(1), pp. 95-111.

Iglauer, S., Paluszny, A. and Blunt, J.M. (2013), "Simultaneous oil recovery and residual gas storage: A pore-level analysis using in situ X-ray micro-tomography", Fuel, 103, pp. 905-914 (http://dx.doi.org/10.1016/j.fuel.2012.06.094)

Kamiya, K. Uno, T., and Matsushima, T. (1996), "Measurement of the distribution of sandy soil void diameter by air intrusion method", Journal of Japan Society of Civil Engineering, No.541/III-35, pp. 189-198. (in Japanese)

Kato, M., Takahashi, M., Kawasaki, S., Mukunoki, T., and Kaneko, K. (2013): "Evaluation of porosity and its variation in porous materials using microfocus x-ray computed tomography considering the partial volume effect", Materials Transactions, 54(9), pp. 1678-1685.

Luis I., Will S., Lysia N., and Josh, C. (2005), "The ITK Software Guide", Second Edition Updated for ITK version 2.4, ITK.

Mayer, A.S. and Miller, C.T. (1993), "An Experimental Investigation of Pore-Scale Distributions of Nonaqueous Phase Liquids at Residual Saturation", Transport in Porous Media, 10, pp. 57-80.

Morrow, N.R., and Songkran, B. (1981), "Effect of viscous and buoyancy forces on non-wetting phase trapping in porous media", Surface Phenomena in Enhanced Oil Recovery, Plenum Press, pp. 387-411.

Mostaghimi, P., Blunt, J. M. and Bijeljic, B. (2013), "Computations of absolute permeability on micro-ct images", Math Geoscience 45, pp. 103-125 (DOI 10.1007/s11004-012-9431-4)

Mualem, Y., (1976), "A new model for predicting the hydraulic conductivity of unsaturated porous media", Water Resources Research, 12, pp. 513-522.

Mukunoki, T. Fujimi, T. and Matsumoto, H. (2014), "Image segmentation and its quantitative evaluation of X-ray CT data of geomaterials using EM algorithm, Japanese Geotechnical Journal, 9

Solid Earth Discuss., doi:10.5194/se-2016-16, 2016
Manuscript under review for journal Solid Earth
Published: 5 February 2016

(4), pp. 555-567. (in Japanese)

Mukunoki, T., Sugimura, K., and Mikami, M. (2010), "Visualization of LNAPL contamination in sandy soil using X-ray CT scanner", Proc. of International Symposium on Earth Science and Technology 2010, pp. 153-158.

Muljadi, B., P., Blunt, J. M. Raeini, Q. A., and Bjijelic, B. (2015), The impact of porous media heterogeneity on non-Darcy flow behavior from pore-scale simulation, Advances in Water Resources, 000, pp. 1-12 (http://dx.doi.org/10.1016/j.advwaters.2015.05.019)

Otani, J. and Obara, Y. edt. (2003), "X-ray CT for Geomaterials soils, concrete, rocks", Proc. of the 1st international workshop on X-ray CT for Geomaterials, GeoX 2003.

Otsu N.(1979), "A Threshold Selection Method from Gray-Level Histograms", IEEE Transactions of Systems, Man, and Cybernetics, 9(1), pp. 62-66.

Pantazidou, M., and Sitar, N. (1993), "Emplacement of nonaqueous liquid in the vadose zone", Water Resources Research, 29(3), pp. 705-722.

Parker, J. C., Lenhard, R. J., and Kuppusamy, T. (1987), "A parametric model for constitutive properties governing multiphase flow in porous media", Water Resources Research, 23(4), pp. 618-624.

Riyadh Al-Raoush (2007), "Microstructure characterization of granular materials", Physica A, 377, pp. 545-558, doi:10.1016/j.physa.2006.11.090

Sato, T., Soba, T. Kuwayama, T and Uno, T. (1992), "Mercury intrusion technique for macropore measurement of particulate soil", Journal of Japan Society of Civil Engineering, No.445/III-18, pp. 139-142. (in Japanese)

Soga, K., Kawabata, J., Kechavarzi, C., Coumoulos, H., and Waduge, W. A. P. (2003), "Centrifuge Modeling of Nonaqueous Phase Liquid Movement and Entrapment in Unsaturated Layered Soils", Journal of Geotechnical and Geoenviromental Engineering, 129(2), pp. 173-182.

Soille, P. (2003), "Morphological image analysis: principles and applications", Springer-Verlag, Berlin Heidelberg, New York.

Taylor, H.F., O'Sullivan, C. and Sim, W.W. (2015), "A new method to identify void constrictions in micro-CT images of sand", Computers and Geotechnics, 69 (2015), pp. 279–290, http://dx.doi.org/10.1016/j.compgeo.2015.05.012

Topp, G. C., and Miller, E. E. (1966), "Hysteretic moisture characteristics and hydraulic conductivities for glass-bead media", Soil Science Society of America, Proceedings, 30, pp. 156-162.

Uno,T. Kamiya, K. and Tanaka, K. (1998), "The distribution of sand void diameter by air intrusion method and moisture characteristic curve method", Journal of Japan Society of Civil Engineering, No.603/III-44, 35-44. (in Japanese)

Wildenschild, D. and Sheppard, P.A. (2013), "X-ray imaging and analysis techniques for quantifying pore-scale structure and processes in subsurface porous medium systems", Advances in Water Resources 51, 217-246, http://dx.doi.org/10.1016/j.advwatres.2012.07.018

Wildenschild, D., Culligan, K.A., and Christensen, B.S.B. (2005), "Application of X-ray micro tomography to environmental fluid flow problems", Proceedings of International Society for Photo-optical Instrumentation Engineers (SPIE): Developments in X-Ray Tomography IV; Ulrich Bonse, pp. 432-441.

Wildenschild, D., Hopmans, J.W., Rivers, M.L., and Kent, A.J. (2005), "Quantitative analysis of flow processes in a sand using synchrotron-based X-ray microtomography", Vadose Zone Journal, 4, pp. 112-126.

Wildenschild, D., Hopmans, J.W., Vaz, C., Rivers, M.L.,Rikard, D., and Christensen, B.S. (2002), "Using X-ray computed micro tomography in hydrology: systems, resolution and limitations", Journal of Hydrology, 267, pp. 285-297.

Solid Earth Discuss., doi:10.5194/se-2016-16, 2016
Manuscript under review for journal Solid Earth
Published: 5 February 2016

Figures

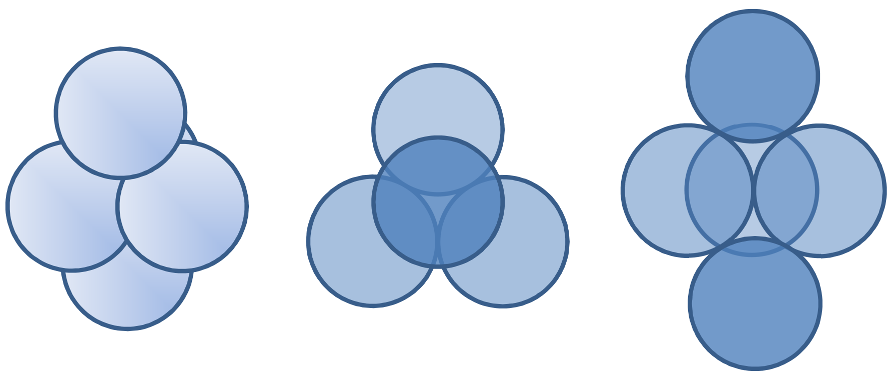

(a) 5 spheres in 3D (b) Plane view of (a) from the top (c) Plane view of (a) from the side

Figure 1: Illustration of spheres for pore surrounded particles

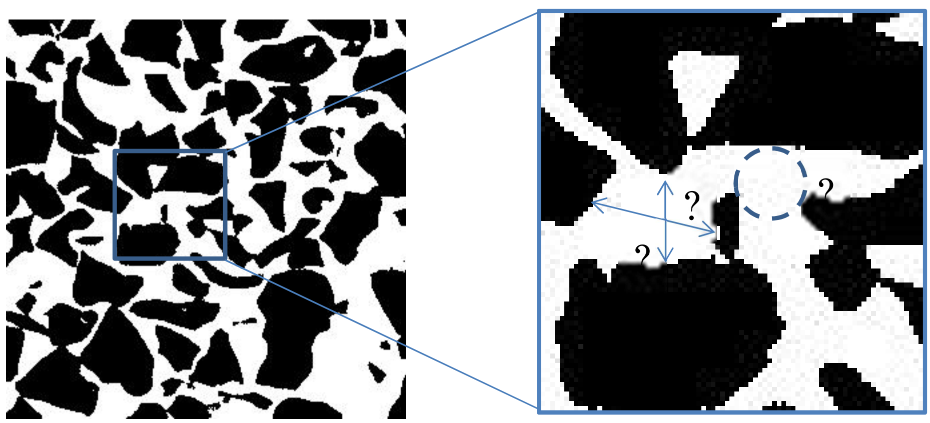

(a) X-ray CT image of grain in 2D (b) Zoomed image

Figure 2 : Binary image of a pore in grains (white indicates pore space and black indicates particles)

Solid Earth Discuss., doi:10.5194/se-2016-16, 2016
Manuscript under review for journal Solid Earth
Published: 5 February 2016

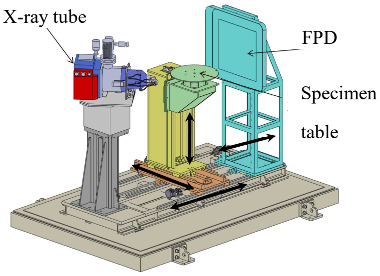

Figure 3: Illustration of micro-focused X-ray CT scanner

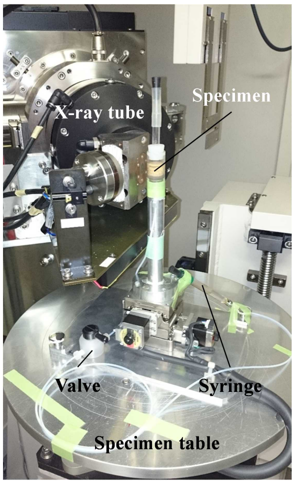

Figure 4: Photograph of a scan scene

Solid Earth Discuss., doi:10.5194/se-2016-16, 2016
Manuscript under review for journal Solid Earth
Published: 5 February 2016

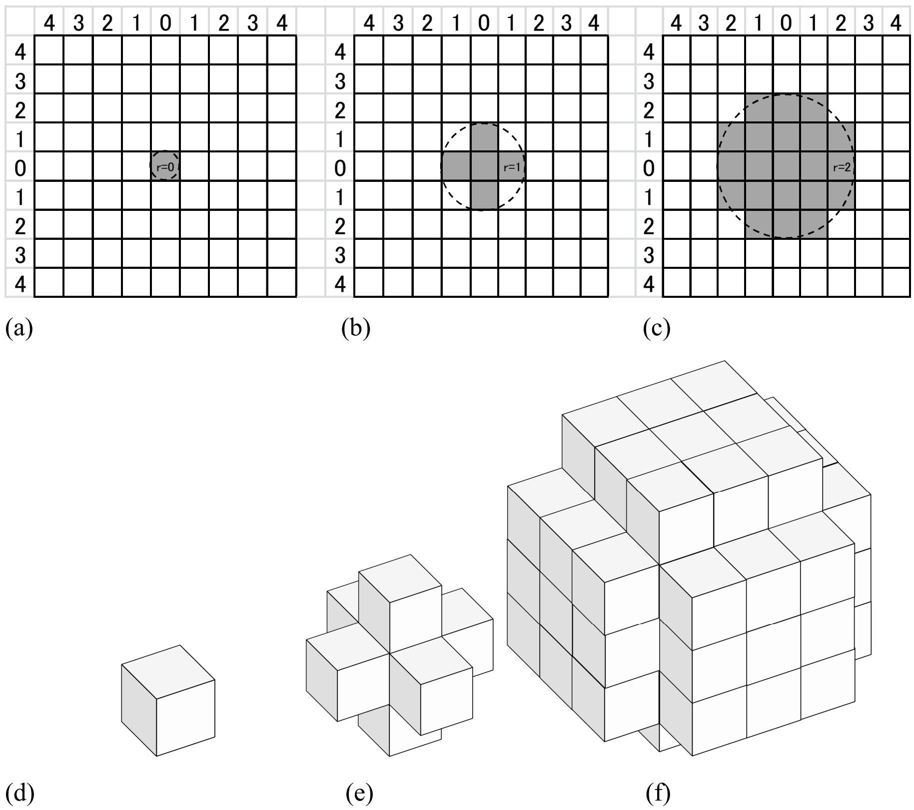

Figure 5: Illustration of sphere elements with different diameters in 2D and 3D views

Solid Earth Discuss., doi:10.5194/se-2016-16, 2016
Manuscript under review for journal Solid Earth
Published: 5 February 2016

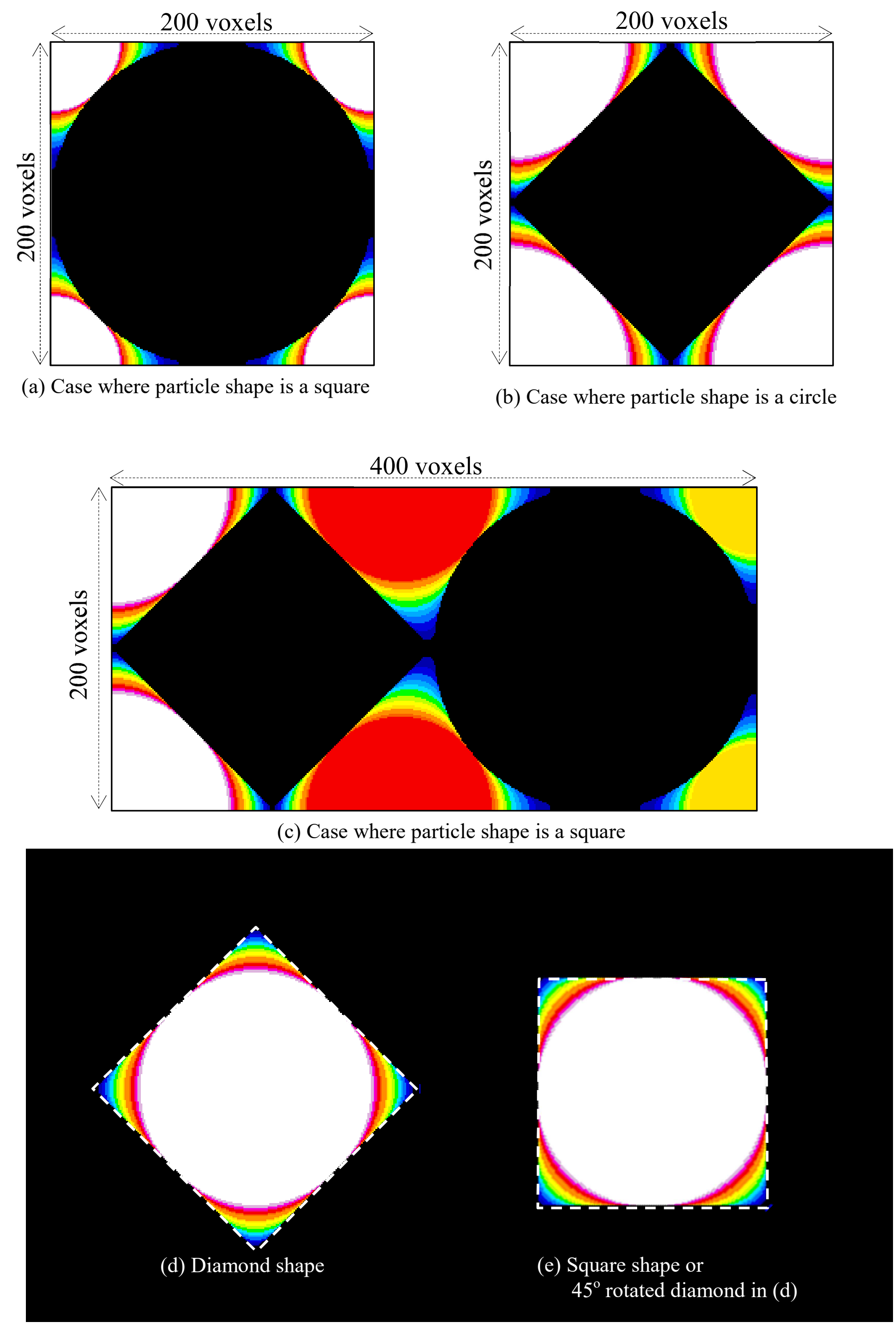

Figure 6: Explanation of features of GMI

Solid Earth Discuss., doi:10.5194/se-2016-16, 2016
Manuscript under review for journal Solid Earth
Published: 5 February 2016

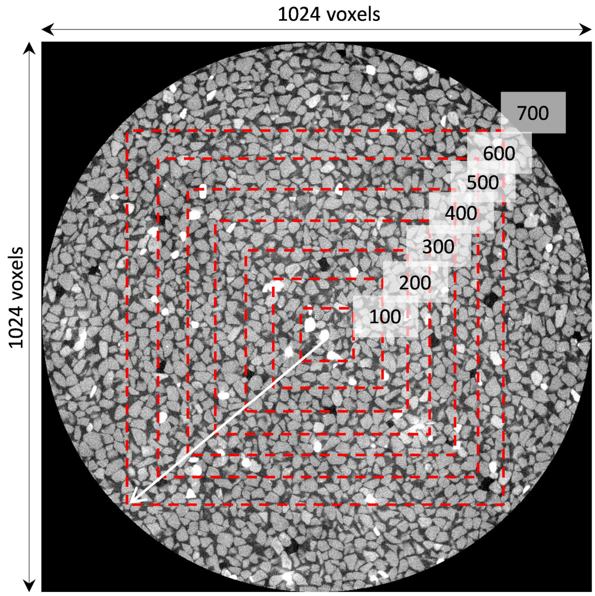

Figure 7(a): X-ray CT image of Toyoura sand with different regions of image analysis in 2D

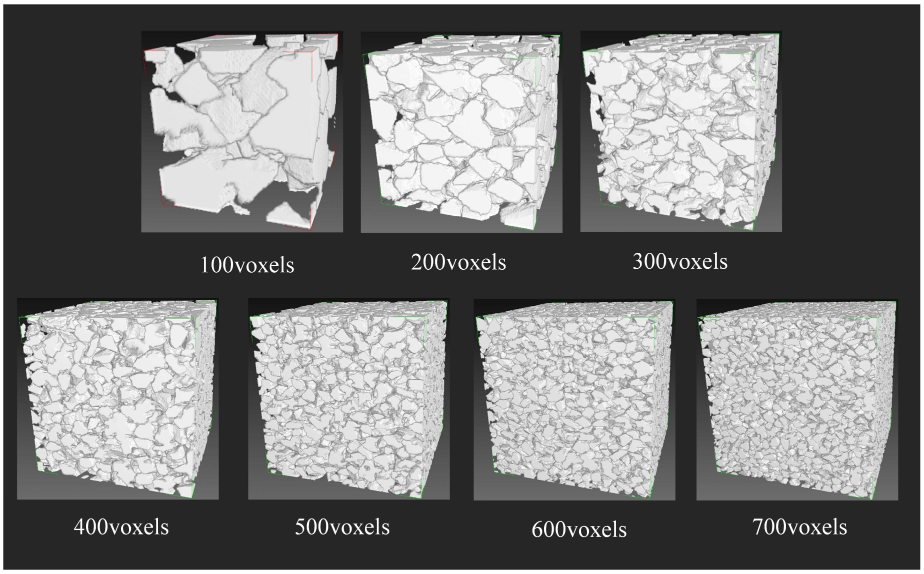

Figure 7(b): X-ray CT image of Toyoura sand with different regions of image analysis in 3D

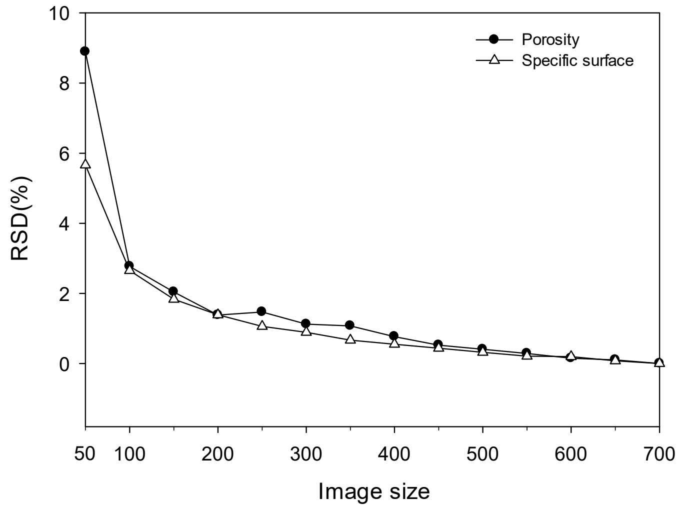

Figure 8: Relative standard deviation by changing the dimension of image analysis

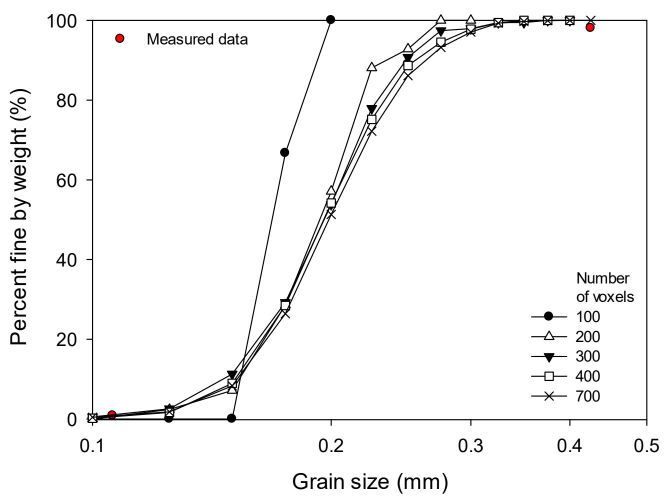

Figure 9: Grain size distribution curve obtained from image analysis

Solid Earth Discuss., doi:10.5194/se-2016-16, 2016
Manuscript under review for journal Solid Earth
Published: 5 February 2016

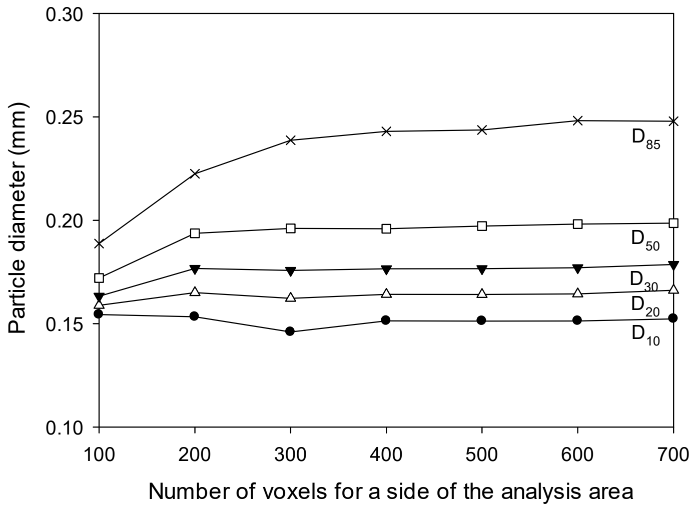

Figure 10: Grain level on each image size

Solid Earth Discuss., doi:10.5194/se-2016-16, 2016
Manuscript under review for journal Solid Earth
Published: 5 February 2016

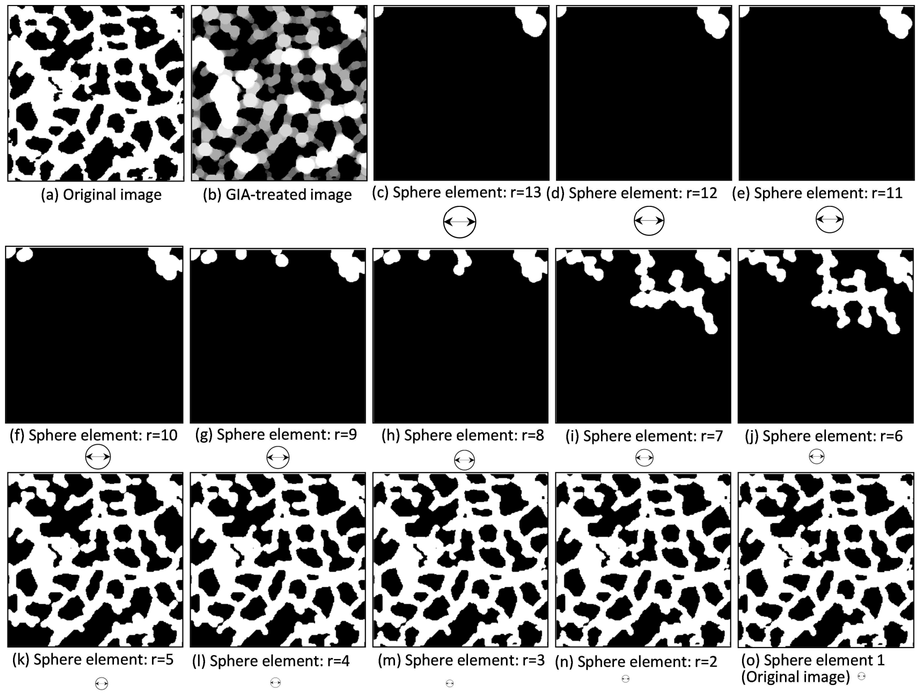

Figure 11: VPM analysis in grains

Solid Earth Discuss., doi:10.5194/se-2016-16, 2016
Manuscript under review for journal Solid Earth
Published: 5 February 2016

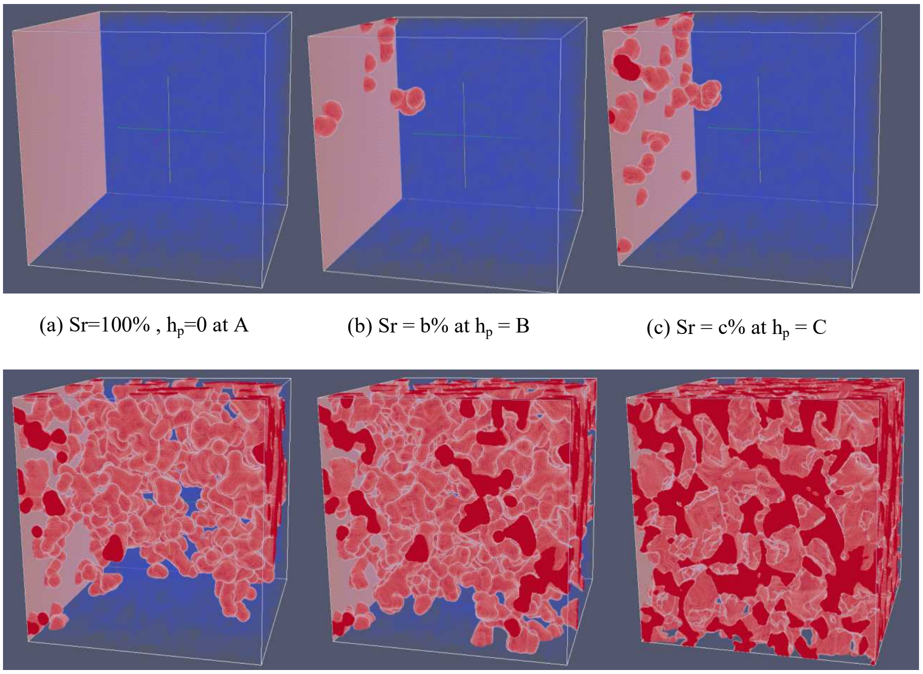

(a) Sr=100% , h_p=0 at A (b) Sr = b% at h_p = B (c) Sr = c% at h_p = C

(d) Sr = d% at h_p = D (e) Sr = e% at h_p = E (f) Sr = f% at h_p = F

Figure 12: Voxel percolation method in grains

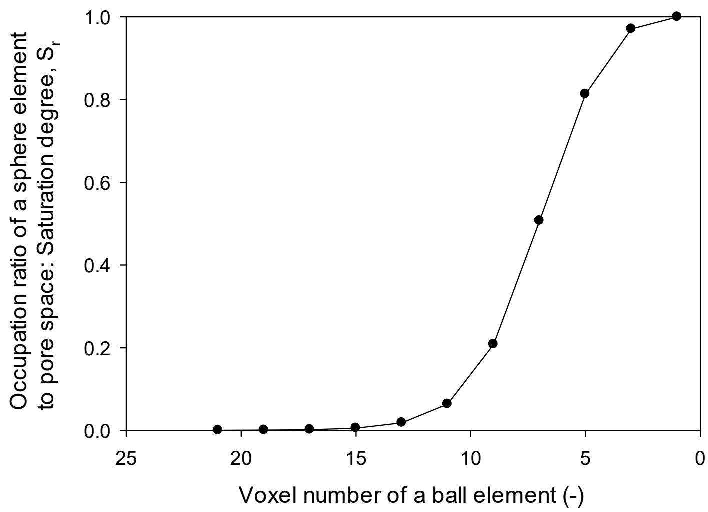

Figure 13: Profile of occupation ratio of the sphere element

Solid Earth Discuss., doi:10.5194/se-2016-16, 2016
Manuscript under review for journal Solid Earth
Published: 5 February 2016

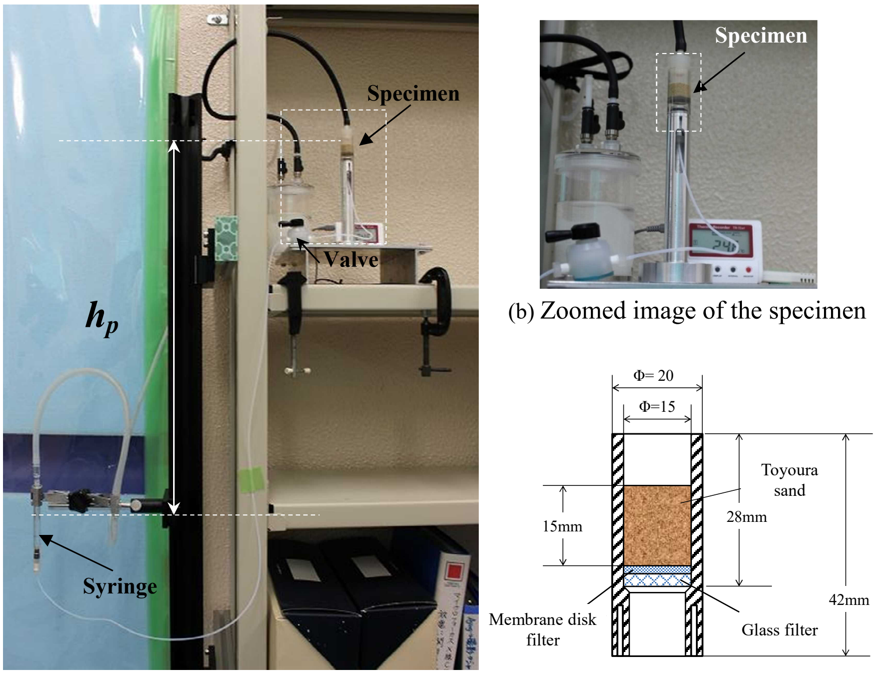

(a) Image of the entire test

(b) Zoomed image of the specimen

(c) Schematic of the test mold

Figure 14: Water retention test apparatus with elevation head method

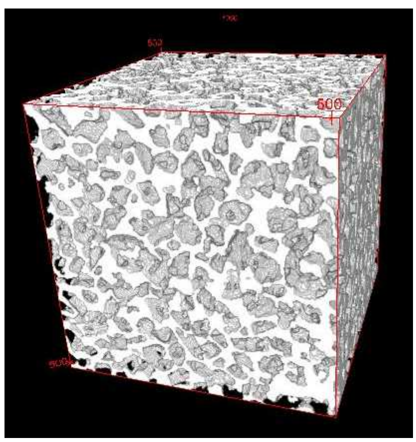

Binary image of pore space for Toyoura sand

Figure 15: X-ray CT image of pore in Toyoura sand in 3D

Solid Earth Discuss., doi:10.5194/se-2016-16, 2016
Manuscript under review for journal Solid Earth
Published: 5 February 2016

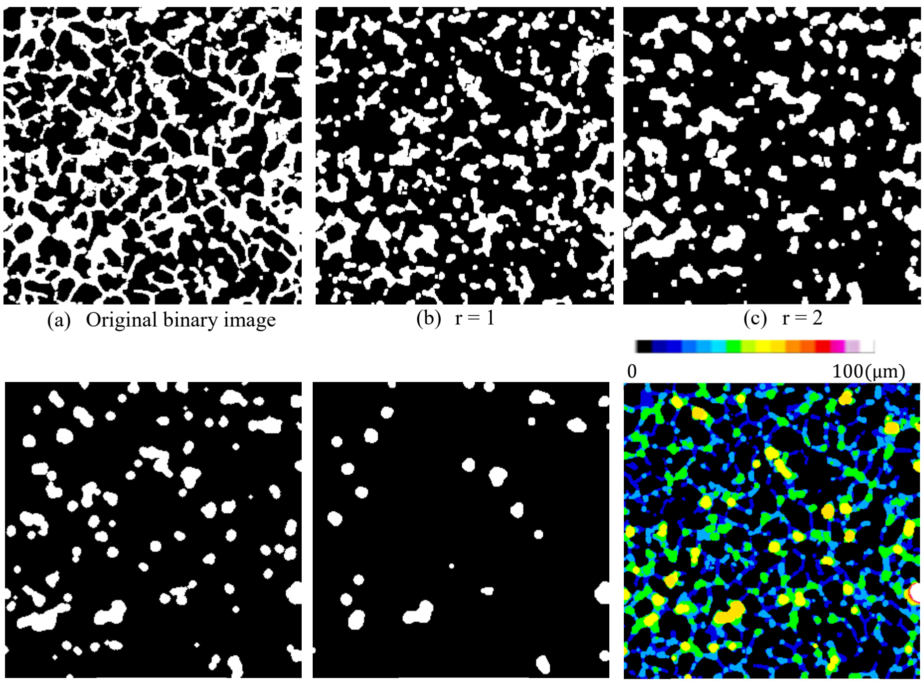

(a) Original binary image (b) r = 1 (c) r = 2

(d) r = 5 (e) r = 10 (f) Map of pore size

Figure 16(a), (b), (c), (d), (e), (f): X-ray CT images obtained from GMI

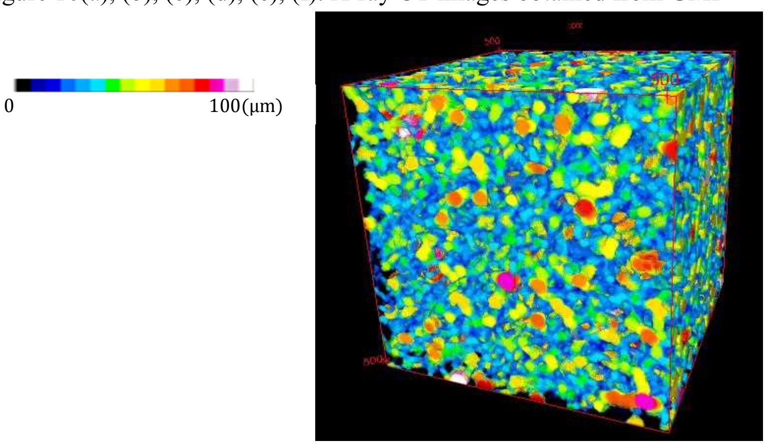

(b) 3D map of pore space for Toyoura sand

Figure 17: Distribution of perforated pore size in 3D

Solid Earth Discuss., doi:10.5194/se-2016-16, 2016
Manuscript under review for journal Solid Earth
Published: 5 February 2016

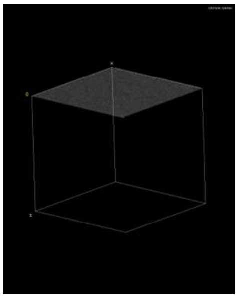

(a) Sr=100% t h_p=0cm

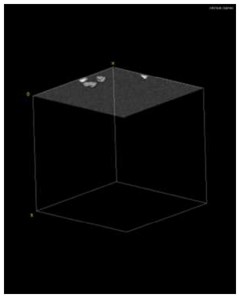

(b) Sr = 99.8% at h_p=19.6 cm

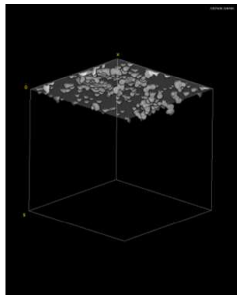

(c) Sr = 99% at h_p=24cm

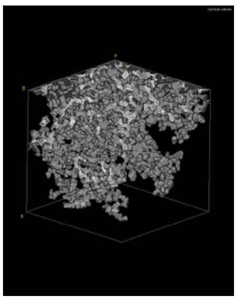

(d) Sr = 80% at h_p = 30.89 cm

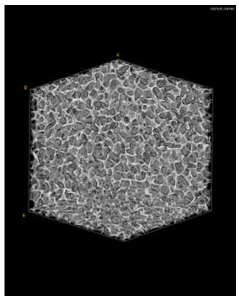

(e) Sr = 28.9% at 43.2cm

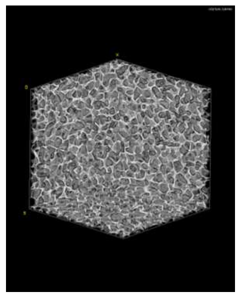

(f) Sr = 3.0% at h_p=72.0 cm

Figure 18: CT images of percolated pore space as the drainage process

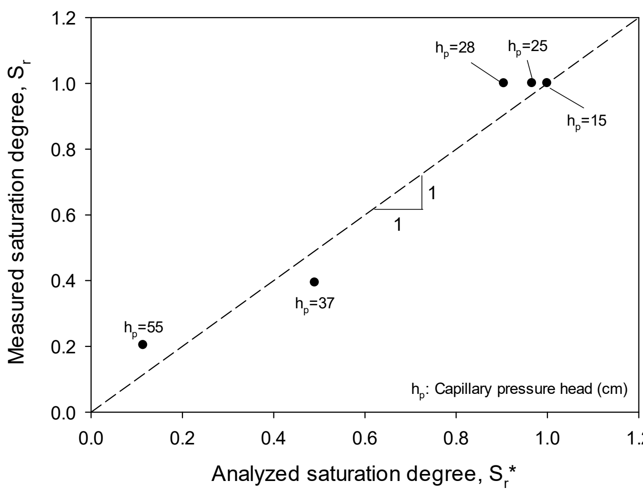

Figure 19: Comparison of saturation degree measured and analyzed at each capillary pressure

Solid Earth Discuss., doi:10.5194/se-2016-16, 2016
Manuscript under review for journal Solid Earth
Published: 5 February 2016

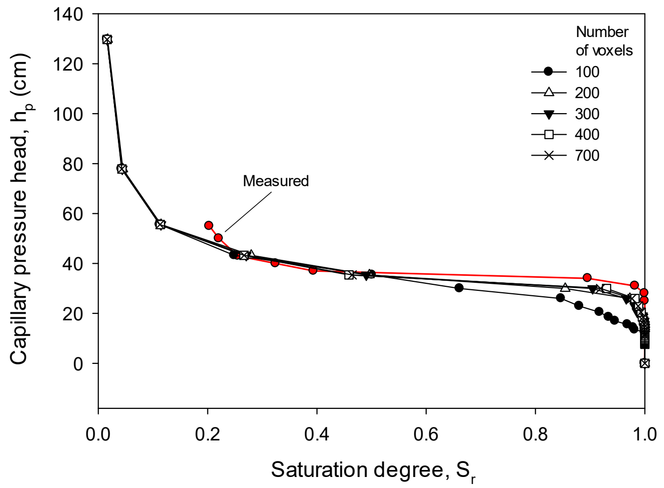

Figure 20: Water retention curves obtained from image analysis and experiment

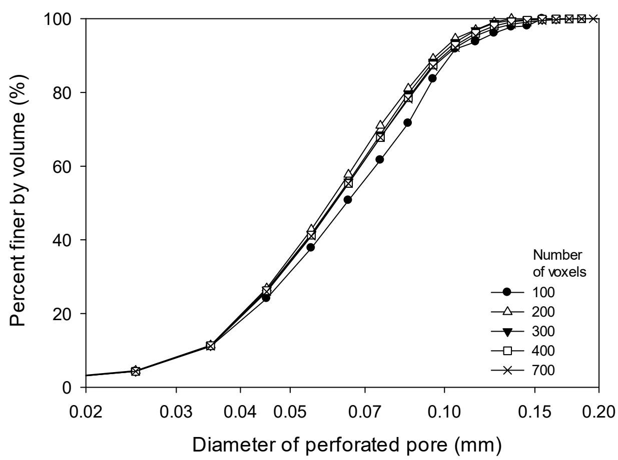

Figure 21: Perforated-pore size distribution for each image size

Solid Earth Discuss., doi:10.5194/se-2016-16, 2016
Manuscript under review for journal Solid Earth
Published: 5 February 2016

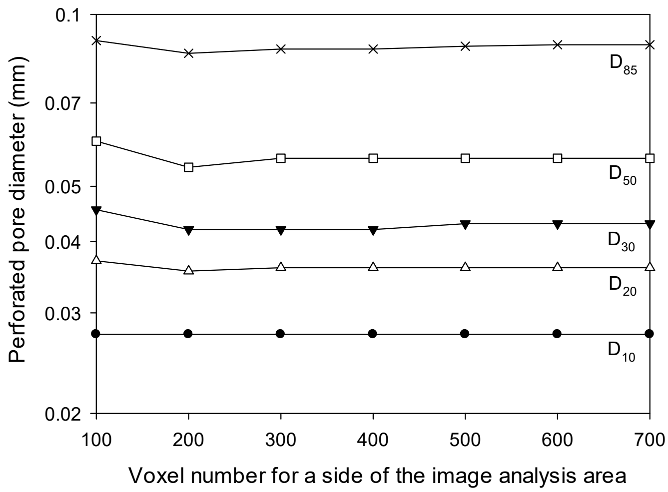

Figure 22: Pore size distribution curve in image size
Figure 22

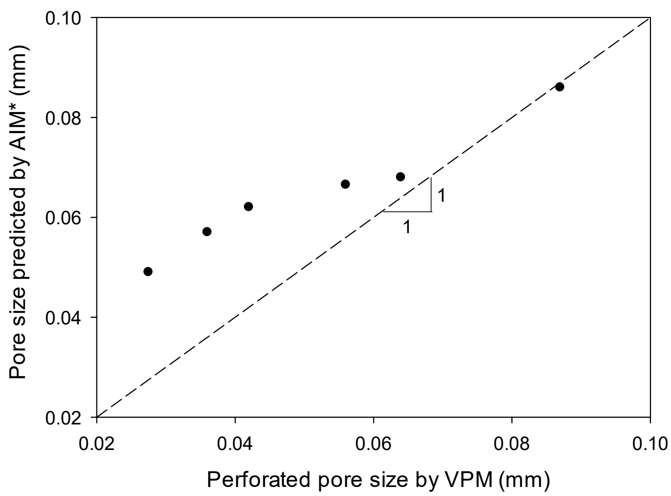

Figure 23: Comparison of pore size obtained from AIM and VPM

Solid Earth Discuss., doi:10.5194/se-2016-16, 2016
Manuscript under review for journal Solid Earth
Published: 5 February 2016

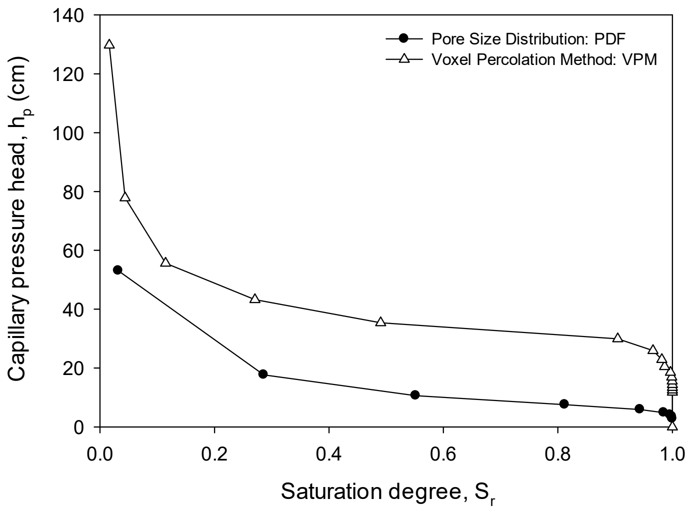

Figure 24: Water retention plots obtained from GMI and VPM

Solid Earth Discuss., doi:10.5194/se-2016-16, 2016
Manuscript under review for journal Solid Earth
Published: 5 February 2016

Table 1 Specifications of a micro-focused CT scanner installed at Kumamoto University

Radiograph field vision	400 mm, height 500 mm
Number of display voxels	1024 x 1024
Resolution	4 µm
Cone bean scan	Normal, Offset, Half
X-ray beam thickness for plain beam	0.2/0.4/0.6/1.0/2.0 mm
Voltage for x-ray generating	240 kV (140W) maximum
Maximum weight for specimen table	245 N
Flat panel detector	Effective pixel number: 2000 x 2000
	Range of vision: 400mm x 400 mm

Table 2 Scan conditions used in this study

Power of voltage (kV)	60
Current (µA)	200
Number of views	1500
Number of integration treatments	10
Voxel dimension (µm) x, y, z	5 x 5 x 5
Number of voxels (x, y, z)	1024 x 1024 x 1000

Table 3 Verification results of GMI

	Voxel counts			Area by calculation			
	Solid	Pore space	Total area	equation	Solid	Pore space	Square error (SE)*
Circle	31428	8572	40000	πr^2 100x100x3.1428	31428	8572	0
Square	19801	20199	40000	L x L 140.716x140.716	19800.99266	20199.00734	$5.393\text{x}10^{-5}$
Square Circle	51229	28771	80000	πr^2 + L x L	51228.9927	28771.0073	$5.329\text{x}10^{-5}$

SE = (Voxel counts – Calculation)^2 for each case

Table 4 Results of REV analysis

	Porosity, Specific surface
RSD < 5 %	L > 900 µm (or 100 voxels)
RSD < 2 %	L > 1800 µm (or 160 voxels)
RSD < 1%	1500 µm (or 300 voxels)